nuclear fusion
IAEA

PAPER • OPEN ACCESS

Turbulent transport in the scrape-off layer of Wendelstein 7-X

To cite this article: Carsten Killer *et al* 2021 *Nucl. Fusion* **61** 096038

OPEN ACCESS
IOP Publishing | International Atomic Energy Agency Nuclear Fusion
Nucl. Fusion **61** (2021) 096038 (9pp) https://doi.org/10.1088/1741-4326/ac1ae3

Turbulent transport in the scrape-off layer of Wendelstein 7-X

Carsten Killer[1,*], **Yann Narbutt**[1], **Olaf Grulke**[1,2] **and the W7-X Team**[a]

[1] Max-Planck-Institut für Plasmaphysik, Wendelsteinstr. 1, 17491 Greifswald, Germany
[2] Department of Physics, Technical University of Denmark, Lyngby, Denmark

E-mail: carsten.killer@ipp.mpg.de

Received 31 May 2021, revised 23 July 2021
Accepted for publication 5 August 2021
Published 24 August 2021

Abstract

Turbulent transport is widely considered to be the main driver for cross-field transport in the scrape-off layer (SOL) of toroidal magnetized plasmas. Here, reciprocating Langmuir probes are employed to measure both the plasma profiles and the turbulent particle transport in the SOL of the Wendelstein 7-X stellarator. The relation between turbulent radial particle flux Γ_r and the local pressure gradient is often approximately linear across the entire SOL width, indicating that radial turbulence spreading is absent. This observation holds across a wide range of magnetic configurations and different plasma heating and density scenarios. The magnitude of the turbulent transport for a given gradient reveals a dependence on the magnetic configuration and the position in the SOL, which we relate to the cross-spectral characteristics of multi-tip floating potential measurements. Magnetic islands can add further complexity due to non-monotonic SOL profiles and the breaking of the transport-gradient relation. Finally, anomalous diffusion coefficients are determined from the probe measurements.

Keywords: stellarator, scrape-off layer, turbulent transport, electric probes

(Some figures may appear in colour only in the online journal)

1. Introduction

The width of the scrape-off layer (SOL) is a fundamental control parameter for the distribution of heat loads onto plasma-facing components in magnetic fusion devices [1, 2]. In general, a wider SOL is considered to be favourable as it distributes heat loads to targets over larger areas. Ideally, the SOL is tailored such that it is wide enough to reduce peak heat loads to acceptable levels while still ensuring that heat loads end up on the 'right' components, i.e. typically the divertor.

Assuming in a simplified picture that the sole source of energy and particles for the SOL is the last closed flux surface (LCFS), the SOL profiles follow from the competition of parallel transport to the divertor vs perpendicular transport across the SOL. The latter process is widely assumed to be dominated by turbulent transport [3–5]. The origin of the turbulence in the SOL, the major mechanisms being the interchange mode and the drift wave, however, is not always clear. Both mechanisms depend on the pressure gradients that are intrinsically present in the SOL. However, numerous investigations report on turbulence activities in regions of the SOL that do not correlate to the local gradients, also called turbulence spreading: in tokamaks, turbulent blob-filaments appear to travel quasi-ballistically from their birth region at the separatrix into the far SOL, where they cause much higher intermittent fluctuation levels than expected from the far SOL plasma conditions [6–9]. In stellarators, (poloidal) turbulence spreading has also been reported, where turbulence spreads poloidally from (interchange) unstable to stable regions [10, 11]. Turbulent transport arising from turbulence spreading is sometimes also called non-local turbulent transport [12].

In the optimized stellarator Wendelstein 7-X (W7-X), plasma filaments have been observed to span long parallel

* Author to whom any correspondence should be addressed.
[a] See Klinger *et al* 2019 (https://doi.org/10.1088/1741-4326/ab03a7) for the W7-X Team.

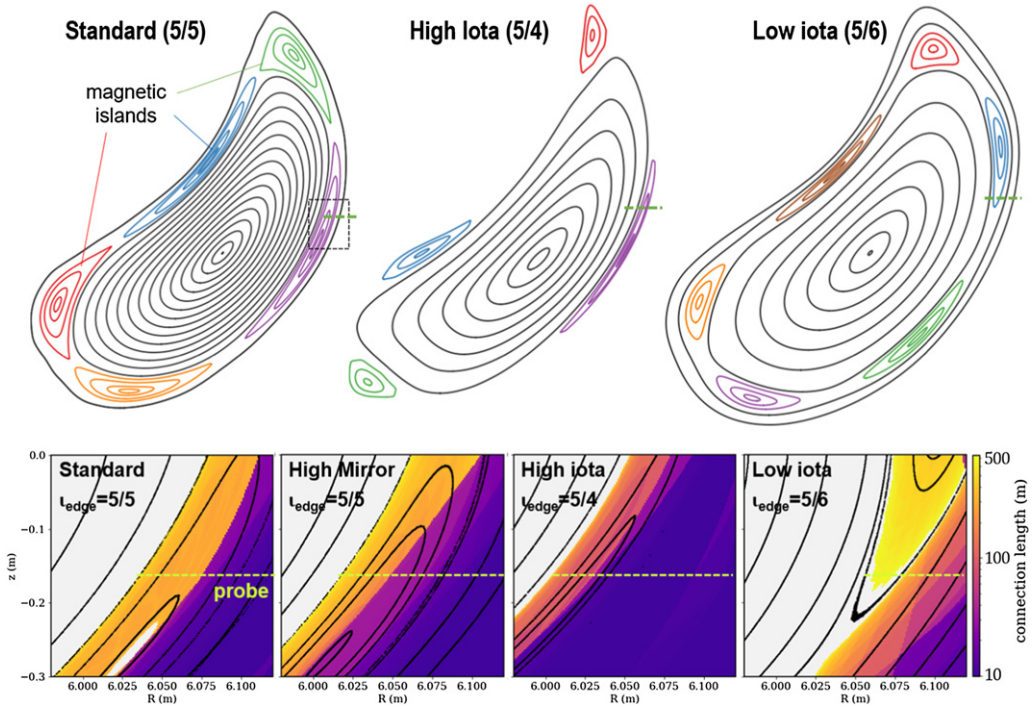

Figure 1. Upper row: Poincaré cross section of different W7-X magnetic configuration in the MPM plane. The major resonant magnetic islands forming the island divertor are highlighted in colours. The probe path is indicated by a dashed green line. Bottom row: Poincare cross section and color-coded connection length (sum of L_c along and against the field) in the vicinity of the MPM.

elongation lengths through regions of strongly varying magnetic curvature [13, 14]. Moreover, due to the 3D nature of the W7-X SOL imposed by the island divertor [15], also the local perpendicular gradients can vary significantly along a field line. In previous investigations, no indications for tokamak-like intermittent transport of blob filaments or radial turbulence spreading have been observed outside of magnetic islands: the probe investigations in Killer *et al* [14] indicate that the SOL turbulence is local, i.e. turbulent structures do not emerge radially from their birth region, as the radial velocities of not more than a few 100 m s^{-1} in conjunction with their lifetime do not allow for a considerable radial turbulence spreading. Consequently, density fluctuations closely resemble normal distributions across the SOL in W7-X [13, 14], which again is in contrast to tokamaks [16, 17]. Agreement of the W7-X observations with modelling indicates that the slow filament velocities in W7-X are mostly due to the smaller magnetic curvature that follows from the large major radius ($R_{\mathrm{major}} \approx 5.5$ m) of W7-X.

The indications for the local character of turbulence observed in the W7-X SOL [14] imply that the magnitude of turbulent transport is expected to scale with the radial plasma pressure gradient that drives the instabilities, i.e. $\Gamma_r \sim \nabla p$ [8, 18]. Here, this hypothesis is tested using reciprocating Langmuir probes mounted on the multi-purpose manipulator (MPM) [19, 20] of W7-X. Exploiting spatially distributed arrangements of multiple probes, profiles of T_e, n (and therefore the pressure gradient) as well as an estimate of radial fluctuating particle transport via $\Gamma_r = \tilde{n}\tilde{v}_r = \tilde{n}\tilde{E}_{\mathrm{pol}}/B$ are obtained. After the experimental setup has been introduced in section 2, the scaling of Γ_r vs ∇p will be assessed across multiple magnetic configurations and a wide range of plasma conditions in section 3. Finally, we briefly consider the description of turbulent transport as a diffusive process which allows to estimate anomalous diffusion coefficients in section 4.

2. Experimental setup

On the low field side of W7-X, the MPM [19] allows to plunge fast reciprocating probes across the SOL. Here, a probe head containing an array of 22 cylindrical Langmuir probe tips is employed, which are arranged such that the array is approximately tangential to the LCFS [20]. The multiple probe tips allow to operate triple probe setups, constant ion saturation current and floating potential measurements as well as classic swept Langmuir probes simultaneously.

2.1. Probe location in the magnetic field of W7-X

While the position of the MPM is fixed, the topology of the magnetic field along the probe path can change as a function of the different magnetic configurations in W7-X. Particularly relevant for the SOL, the chain of magnetic islands forming the island divertor concept [21] varies as a function of the rotational transform ι. The location of the probe path w.r.t. the island chain is presented in figure 1 for the three major island divertor configurations ($\iota_{\mathrm{edge}} = 5/5, 5/4, 5/6$, respectively). In the standard and high iota configuration, the probe scans through one of the magnetic islands, slightly above the O point. In the low iota configuration, the probe path barely intersects the island, slightly above an X point. In addition to these situations, so-called limited configurations can be created by

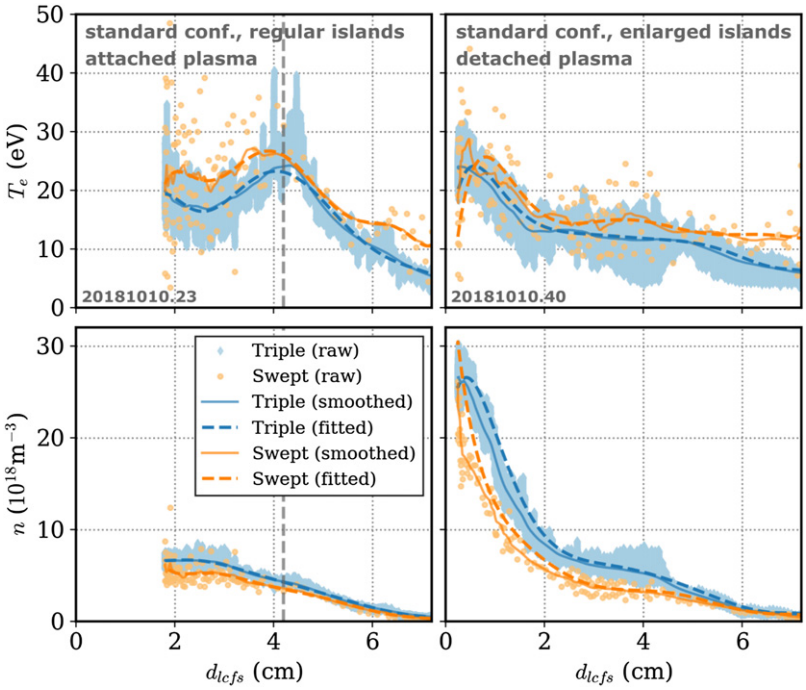

Figure 2. Comparison of T_e and n profiles from triple probe (blue) and swept probe (orange). The smoothed data is lowpass-filtered and the fitted data is represented by an 8th order polynomial. The vertical dashed line indicates the L_c transition in the standard configuration with regular islands.

setting ι_{edge} such that there is no island chain at the edge, so that nested closed flux surfaces extend up to the divertor targets, which then act as limiters [22]. The bottom row in figure 1 shows the local vicinity of the reciprocating probe with the connection lengths to the targets being color-coded.

2.2. T_e and n profiles

To increase confidence about the Langmuir probe results, both classic swept Langmuir probes as well as triple probe arrangements have been employed to determine T_e and n [23, 24]. The swept Langmuir probe has the advantage of a more accurate model (measuring the entire I–V curve), to the expense of a low temporal resolution (and therefore low spatial resolution as the probe moves) due to the limited sweeping frequency. The triple probe, in contrast, operates faster (at the speed of data acquisition) but uses a rougher simplification of the I–V curve model.

Typical results of both techniques in two measurements in the magnetic standard configuration are presented in figure 2. Both probe methods usually agree qualitatively, although the swept probe mostly provides higher T_e and smaller n compared to the triple probe. As the swept probe has a stronger scatter and unreasonably high temperatures in the far SOL at $d_{LCFS} > 7$ cm (due to high fluctuation levels in the raw data that make it difficult to identify the transition between electron and ion branch of the I–V curve), we use the triple probe for all further computations in this work. The swept probe results are considered as a qualitative confirmation of the triple probe scheme.

Finally, the T_e and n profiles are approximated by an 8th order polynomial for further processing (gradient calculation) and better handling of large amounts of experiments in a data base. The relatively high order of the polynomial is required to accurately reflect fine structures of the profiles that are associated with the magnetic islands, see e.g. the characteristic T_e peak at $d_{LCFS} \approx 4$ cm in figure 2 top left panel.

2.3. Fluctuation measurements, estimation of perpendicular fluctuating transport

The reciprocating electric probes have further been used to measure plasma fluctuations with a sampling rate of typically 2 MHz. In particular, several pins on the poloidal array [14, 20] have been operated in floating potential (V_{fl}) mode or at a constant negative bias voltage (collecting ion saturation current $I_{i,sat}$). Considering a set of three pins with the $I_{i,sat}$ pin in the centre and V_{fl} pins above and below it, density (via $I_{i,sat}$ pin) and V_{fl} fluctuations can be obtained simultaneously. The fluctuating poloidal electric field across the position of the density measurement is estimated by $E_{pol} = (V_{fl,upper} - V_{fl,lower})/d_{pins}$ with the sign convention such that a positive E_{pol} points downwards, resulting in a radially outwards $E_{pol} \times B$ drift at the LFS with the usually ccw magnetic field direction of W7-X. The probe pins have a diameter of 2 mm and a (poloidal) spacing of 5 mm between adjacent pins, which is both much larger than typical dispersion scales/ion gyro-radii of 200–300 μm.

T_e fluctuations have been neglected here, as previous experiments have shown that they are usually small and to the degree of the spatial accuracy of the probe head approximately in phase with the potential fluctuations, legitimizing this simplification [14]. The radial velocity follows directly by $v_r = (E_{pol} \times B)/B^2$ and the fluctuating radial particle

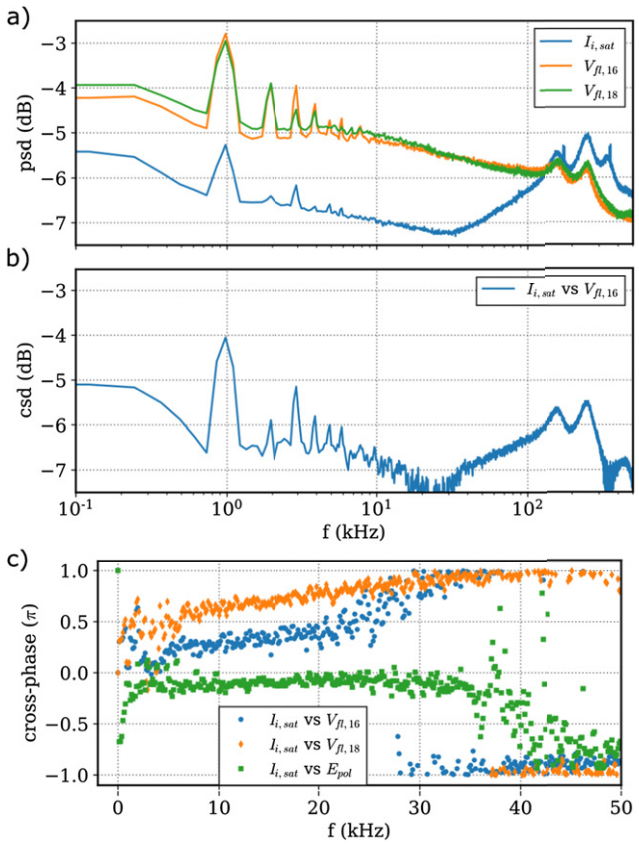

Figure 3. Spectral characteristics of typical $I_{\mathrm{i,sat}}$ and V_{fl} data in a 1000 ms measurement with a constant probe position in the low iota configuration. (*a*) Power spectral density, (*b*) cross spectral density, (*c*) cross-phase.

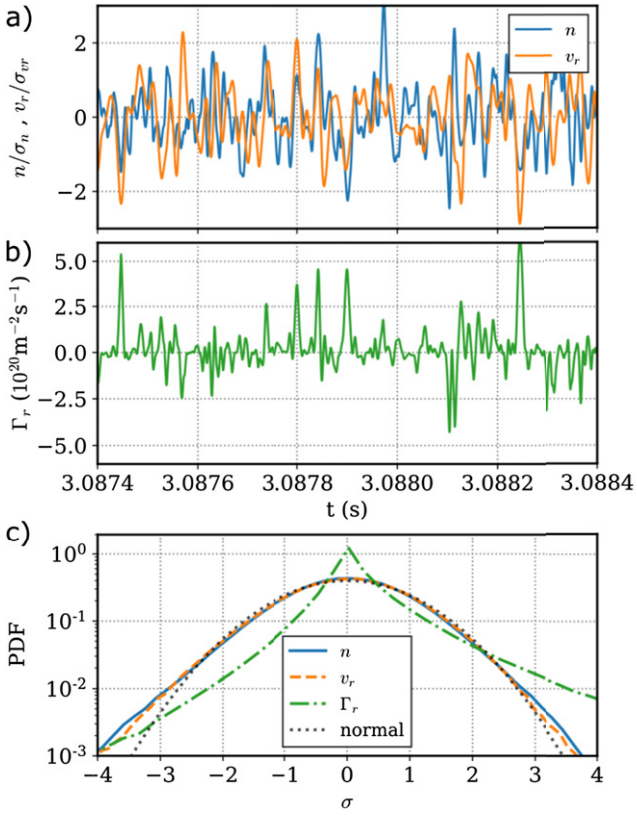

Figure 4. Example time traces of (*a*) fluctuating n, v_{r}, and (*b*) Γ_{r}. (*c*) Histogram of $\tilde{n}$ (red), $\tilde{v}_{\mathrm{r}}$ (green) and Γ_{r} (blue) fluctuations. A normal distribution is shown in black for comparison.

transport is finally estimated as $\Gamma_{\mathrm{r}} = \tilde{n}\tilde{v}_{\mathrm{r}} = \tilde{n}\tilde{E}_{\mathrm{pol}}/B$, neglecting the magnetic flutter transport contribution.

For these calculations, only the spectral range of 5 kHz to 50 kHz was considered by applying band-pass Butterworth filters to the raw data. This decision is motivated by the spectral characteristics of the raw data that is exemplarily presented in figure 3. The power density spectra (PSD) of $I_{\mathrm{i,sat}}$ and V_{fl} data in figure 3(*a*)) show an increase of the PSD towards higher frequencies starting at 30–50 kHz and typically peak in the region between 150 kHz and 300 kHz. Such a behaviour is not expected from purely turbulent fluctuations and is presumably due to (possibly Alfvenic []) mode activity. On the lower frequency end of the spectrum, the influence of the nearby swept probe operating at 1 kHz (including harmonics) is clearly seen and can thus perturb the fluctuations measurements. Therefore, both the low (typically <5 kHz, which also encompasses diamagnetic and $E_{\mathrm{r}} \times B$ frequencies) and high (typically >50 kHz) frequency range is excluded from further analysis.

The cross-phase is particularly relevant for the particle transport from density and v_{r} fluctuations and for the identification of the underlying instabilities. It is presented in figure 3(*c*)) for the relevant spectral range only for visual clarity. In the frequency range of a few 10 kHz, the cross-phase between $I_{\mathrm{i,sat}}$ ($\sim n$) and E_{pol} ($\sim v_{\mathrm{r}}$) is $\approx$0, maximizing

Table 1. Fluctuation statistics corresponding to figure 4(*b*)). (Kurtosis = 0 for a normal distribution.)

Quantity	Mean	σ	Skewness	Kurtosis
n	0	0.84×10^{18}m^{-3}	−0.11	0.95
v_{r}	0	185 m s^{-1}	−0.10	0.49
Γ_{r}	0.24σ	1.72×10^{20}m^{-2} s^{-1}	1.95	15.02

the outwards particle transport for given $I_{\mathrm{i,sat}}$ and E_{pol} fluctuation amplitudes. In the same spectral range, the cross-phase between $I_{\mathrm{i,sat}}$ and V_{fl} is roughly in the region of $\pi/2$, revealing an interchange-type character of the observed fluctuations. While the PSD and CSD are qualitatively representative for the vast majority of the available data, the cross-phase and cross-coherence can change significantly as a function of magnetic configuration and measurement position, which will be discussed in section 3.2.

The paramount role of the cross phase for the resulting particle transport is further showcased in the exemplary time traces of the fluctuating density $\tilde{n}$ and fluctuating $\tilde{v}_{\mathrm{r}}$ as well as their product $\Gamma_{\mathrm{r}} = \tilde{n}\tilde{v}_{\mathrm{r}}$ in figure 4(*a*)). While $\tilde{n}$ and $\tilde{v}_{\mathrm{r}}$ show similar levels of positive and negative fluctuations, Γ_{r} features much more positive events, indicating a bias towards outwards directed particle transport. This observation is further solidified in the probability distribution functions of these three

quantities presented in figure 4(*b*)) and the associated statistical moments listed in table 1. While $\tilde{n}$ and $\tilde{v}_r$ closely resemble normal distributions (in agreement with earlier investigations in the W7-X SOL [13, 14]), Γ_r is characterized by positive skewness and positive (excess) kurtosis. This is due to the cross phase between $\tilde{n}$ and $\tilde{v}_r$ and indicates a tendency towards positive (outwards) particle transport with an increased occurrence of large transport events.

3. Turbulent transport vs local gradients

Due to the absence of turbulence spreading in the SOL of W7-X in [14], the magnitude of turbulent transport is expected to directly depend on the local plasma gradients. Without specifying the underlying instabilities, we first consider the plasma pressure gradient, i.e. test the relation $\Gamma_r \sim \nabla p$. In figure 5, the turbulent particle transport Γ_r is presented as a function of ∇p. The data from more than 200 reciprocating probe measurements is distinguished by magnetic configuration and each data point represents the averaged transport over a 5 ms interval, in which the probe does not move more than 2 mm. The data points cover a wide range of (ECR) heating powers ([1–6] MW) and line integrated densities ([2–12] $\times 10^{19}$ m^{-2}) and are taken over the SOL from the LCFS (if the probe moved that far) up to 5 cm outside the LCFS.

In general, a linear relation $\Gamma_r \sim \nabla p$ is seen in most configurations, particularly in the high mirror, high iota, low iota configurations, supporting the hypothesis of local turbulent transport. In these three configurations, the high mirror and low iota cases feature a much larger slope of the linear relation compared to the high iota configuration, implying a systematic configuration dependence of the turbulent transport for a given pressure gradient. The limiter configurations [22] in the rightmost panel also indicate a configuration dependence, with stronger scatter towards higher transport levels for the $\iota < 1$ configurations.

Finally, the standard configuration results in the leftmost panel display a more complex picture. The data is by colour further distinguished into experiments with 'regular' sized magnetic islands (without using the island control coils, i.e. $I_{cc} = 0$, blue) and enlarged islands ($I_{cc} = +[1–2.5]$ kA, red). For the $I_{cc} > 0$ data, again a roughly linear relation $\Gamma_r \sim \nabla p$ is observed. The $I_{cc} = 0$ data, however, reveals a much larger scatter. While still mostly positive (outwards) transport is observed, the quantitative relation to the (sometimes even negative) pressure gradients is not clear. It is interesting to note that particularly in the standard configuration with $I_{cc} = 0$ differences in the SOL profiles across the magnetic islands have been reported. Observations include non-monotonic T_e profiles [15, 20, 25, 26], a poloidal plasma rotation around the islands due to an 'island radial electric field' [20, 27], and a still unexplained fast correlation of plasma fluctuations between inboard and outboard side of an island [13]. The large scatter in the $I_{cc} = 0$ data in figure 5 further emphasizes the additional complexity that magnetic islands can entail.

In the following subsections, a few possible reasons for the unclear flux-gradient relation in the standard configuration at $I_{cc} = 0$ and for the configuration dependence of the linear slopes in the other configurations in figure 5 will be discussed.

3.1. Magnetic field characteristics

Assuming interchange-type turbulence, magnetic field characteristics affect both the origin of the turbulence (normal curvature) and the dissipation of turbulent fluctuations (connection length to target) [8].

While the normal curvature in W7-X has strong, fine-scale variations along a magnetic flux tube [14, 28], previous work has indicated that due to the fast dynamics parallel to the ambient magnetic field, the averaged normal curvature along a field line dominates the formation and behaviour of turbulent filaments [14, 29]. Since the magnetic configurations of W7-X considered here mostly differ with respect to the rotational transform, the magnetic curvature profile along a field line starting from the probe does not change more than a few % between configurations. Assuming that indeed the averaged curvature determines the SOL turbulence, no configuration-dependent effect is expected for the growth of interchange-type turbulence in our measurements.

The connection length to the targets L_c varies quite significantly between different W7-X configurations (see figure 1) and is important as it affects the radial velocity ($v_r \sim L_c$ in sheath-limited regime) and dissipation of turbulent filaments [8].

To investigate the systematic differences between turbulent transport levels in different magnetic configurations, the role of L_c is investigated in figure 6. There, the same data as in figure 5 is shown (in smaller axis limits) with the connection length for each data point colour coded. Since the connection length can be determined in both parallel directions, along and against the magnetic field, the upper row represents the shorter connection length and the lower row the longer one. Intuitively, one would expect the shorter connection length to play the more important role for the behaviour of turbulent structures as this determines the current closure and therefore propagation of a turbulent filament.

However, the connection length does not offer a clear insight into the systematic differences between configurations. Comparing the high iota case with smaller transport per pressure gradient to the high mirror and low iota cases with larger transport per pressure gradient, no clear relation to the connection length is seen. If at all, the high iota case has (for the shorter direction) longer connection lengths. Similarly, the connection length does not relate to the large spread of transport levels for the different limiter configurations, which all show generally small connection lengths.

In the standard configuration, however, the connection length appears to at least correlate to the rather confusing $\Gamma_r \sim \nabla p$ relation: for short L_c in both directions, i.e. in the shadowed region of the island and the private flux region outside the island (see figure 1), a roughly linear relation $\Gamma_r \sim \nabla p$ similar to the other configurations is seen. For data points just inside the main island SOL with very long connection lengths (>200 m in the long direction), significant Γ_r levels are observed even at low pressure gradients <10 Pa cm^{-1}. As

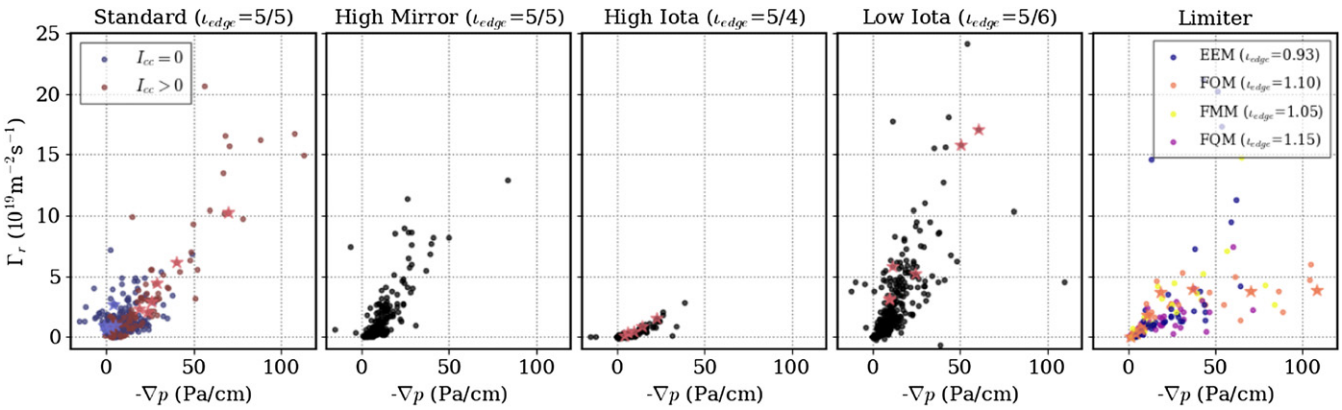

Figure 5. Scatter plot of turbulent radial particle flux as a function of radial plasma pressure gradient distinguished by magnetic configuration. Each dot represents a 5 ms time slice of probe data, covering a wide range of heating and fuelling scenarios and $0 < d_{\mathrm{LCFS}} < 5$ cm. The star symbols represent data points belonging to the experiments presented in figure 7.

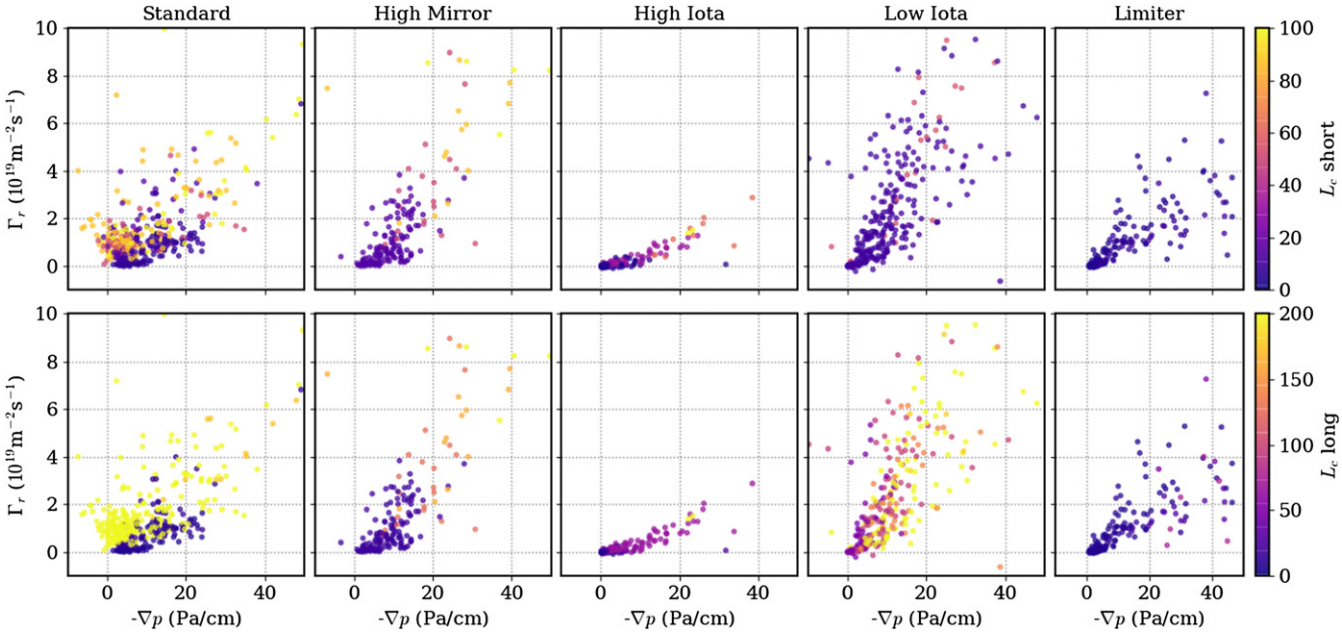

Figure 6. Same data as in figure 5 in different axis limits with connection lengths to the targets color-coded. The upper (lower) row shows the shorter (longer) connection lengths to the target.

indicated in figures 2, 7 and 9 (and [15, 20, 25, 26]), the plasma profiles taken by the reciprocating probe in the standard configuration often feature a local maximum of T_e and a flattening of n at the transition region between the shadowed region with short L_c and the main island SOL with long L_c, resulting in small (or even slightly negative) pressure gradients. This observation might indicate poloidal turbulence spreading in the magnetic islands [13], which, however, cannot be verified without improved diagnostic coverage in upcoming operation phases of W7-X.

3.2. Turbulence characteristics

As discussed in section 2.3, the turbulent particle transport Γ_r depends both on the fluctuation amplitudes and on the cross phase between the individual quantities. The radial profiles of plasma conditions and fluctuation amplitudes/cross phases for five representative experiments in different magnetic configurations in figure 7 will give further insight into the different transport levels between configurations and probe positions.

Starting with the centre column in low iota configuration, the fluctuation amplitudes of n, V_{fl} and E_{pol} all increase towards the LCFS. As the phase between n and E_{pol} is generally ≈ 0 in all configurations (see figure 3), the turbulent particle transport is maximized given the observed fluctuation levels (compare to the high Γ_r in low iota configuration in figure 5).

In the high iota configuration, the fluctuation amplitudes of n and V_{fl} also increase towards the LCFS. However, the E_{pol} amplitude is here much smaller since the two floating potential pins (from which E_{pol} is deduced) are almost perfectly in phase, with a high coherence. Consequently, the turbulent particle transport will be small, see high iota panel in figure 5.

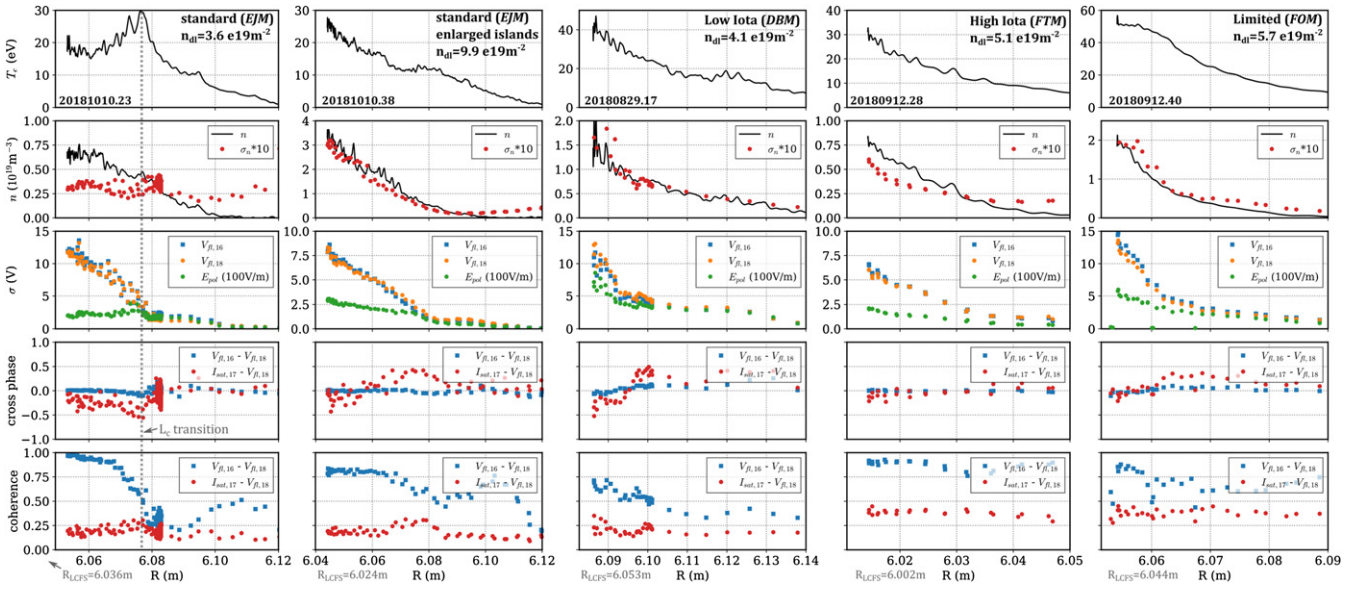

Figure 7. Radial profiles of key quantities along the MPM path (cf figure 1) for five measurements representing different magnetic configurations. All experiments were performed in ECR heated hydrogen plasmas with heating powers between 4 MW and 5.5 MW. The fluctuation amplitudes σ, cross-phase and coherence are evaluated in the frequency range between 3 kHz and 30 kHz. The turbulent particle transport from these experiments is highlighted by star symbols in figure 5.

A similar observation can be made in the limiter configuration in the rightmost panel. Moving closer towards the LCFS, the relative magnitude of E_{pol} fluctuations compared to V_{fl} fluctuations decreases due to an increasingly coherent, in-phase behaviour of the two floating potential measurements. Again, this behaviour results in reduced turbulent transport levels even at stronger pressure gradients, see the star symbols in the rightmost panel in figure 5.

Considering finally the more complicated standard configuration, again the importance of the island size manipulation with control coils is evident. For the enlarged island case in the second column, T_{e} increases monotonically towards the LCFS and $\sigma_n/n \approx 0.1$ throughout the entire SOL. Again, while the V_{fl} fluctuation amplitudes increase similarly to n fluctuations towards the LCFS, the E_{pol} fluctuations show a much smaller increase due to highly coherent in-phase fluctuations of both V_{fl} pins towards the LCFS. For the case with regular magnetic islands in the leftmost panel, again the well-known T_{e} peak at the L_{c} transition between shadowed SOL and main SOL is seen. In the main island SOL (left of that peak), the relative density fluctuations decrease while the V_{fl} fluctuations increase quite strongly. However, again due to the highly coherent in-phase fluctuation of the V_{fl} pins, E_{pol} fluctuations become particularly small here.

Concluding, in most situations the fluctuation amplitudes of n and V_{fl} increase towards the LCFS, whereas E_{pol} (which drives the turbulent particle transport) does not increase as strongly and furthermore shows a dependence on the magnetic configuration and the position in the SOL.

3.3. Diagnostic limitations

The probe array of poloidally aligned probe tips with a finite distance has intrinsic uncertainties: the alignment of the probe array to the magnetic field was chosen such that the array is tangential to the LCFS. While the flux surface shape varies slightly between configurations, the alignment error is not more than 2° for the configurations considered here. In the magnetic islands, which have their own flux surfaces, however, the alignment of the probe array breaks down. In the worst case, close to the island O point, the definition of *radial* (from probe movement) and *poloidal* (from probe array) switch places in the island's own magnetic geometry. Therefore, the particle transport measured by the probe (following section 2.3) would not be *radial* but rather *poloidal* on an island flux surface. However, this issue is restricted to only a narrow part (<1 cm) of the probe path close to the island centre and is not reflected in the data (see e.g. leftmost column of figure 7).

Similarly to the poloidal array potentially loosing its meaning in the magnetic island, the radial pressure gradients obtained from the reciprocating movement of the probe might not show the major directions of the pressure gradients in the magnetic island SOL [15, 20, 25, 26]. Finally, the analysis of plasma fluctuations with a probe array is only sensitive to typical structure sizes of the order of magnitude of the pin separation. A possible interpretation of the increasingly coherent in-phase fluctuations of V_{fl} pins close to the LCFS is that the turbulent structures become much larger (in the poloidal direction) than the distance between probes. Indeed, using other V_{fl} pins with a larger poloidal distance to the central $I_{\mathrm{i,sat}}$ pin yields somewhat larger E_{pol} results in those situations. This observation might, however, also be explained by the slightly decreasing coherence between more distant pin pairs, as the phase remains still very close to 0 in these cases. For further insight into this phenomenon, experiments with larger poloidal probe arrays are planned for the upcoming operation phase of W7-X.

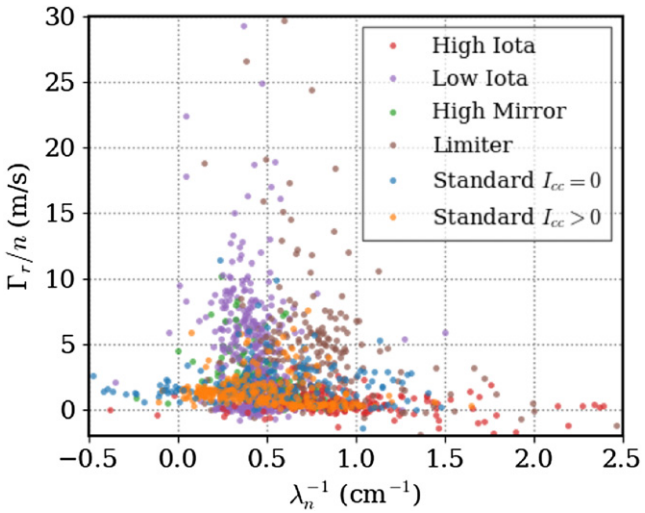

Figure 8. Same data as figures 5 and 6 presented as a function of the generalized Fick's law $\Gamma_r/n = v_0 - D\nabla n/n$ with $\lambda_n = n/\nabla n$.

Summarizing the quantifiable uncertainties in determining Γ_r (and therefore also D in section 4), we find that the choice of different spectral bandpass filter ranges (see section 2.3) and the choice of the pin combination on the probe head [14] can change Γ_r (and D) by up to 50%. This is not a general systematic error as the magnitude and even direction of the error varies between different magnetic configurations and plasma scenarios.

4. Turbulent transport as a diffusive process

The nature of turbulent transport in the SOL can be described as either convective, diffusive, or a combinations of both [30, 31]. While the convective character applies to individual turbulent filaments/blobs, a purely diffusive description is often employed (for modelling purposes) when sufficiently long time series are considered, such that individual convective events are just part of the total time-averaged transport [4, 32]. As an example for modelling applications, the anomalous diffusion coefficient is an integral input parameter into global simulations such as EMC3-EIRENE [33–36].

In figure 8, the same data from figures 5 and 6 is presented in terms of a generalized Fick's law with both convective and diffusive contributions $\Gamma_r = nv_0 - D\nabla n$, with the convective velocity v_0 and the anomalous diffusion coefficient D. In this representation, the intersection of a linear fit with the vertical axis would indicate a convective transport contribution v_0. As no clear indication of a significant convective velocity v_0 is seen here, (but also in tokamaks, this flux-gradient relation is often not very clear [30, 31]), we now simply determine diffusion coefficients via $D = \Gamma_r/\nabla n$ for comparison with EMC3-EIRENE modelling.

Radial profiles of D along with fundamental properties T_e, n, ∇T_e, ∇n, Γ_r are presented in figure 9 for different magnetic configurations/plasma scenarios. For visual clarity, only one data set is shown per scenario. Since not all data sets were at similar experimental conditions (heating, fuelling), the

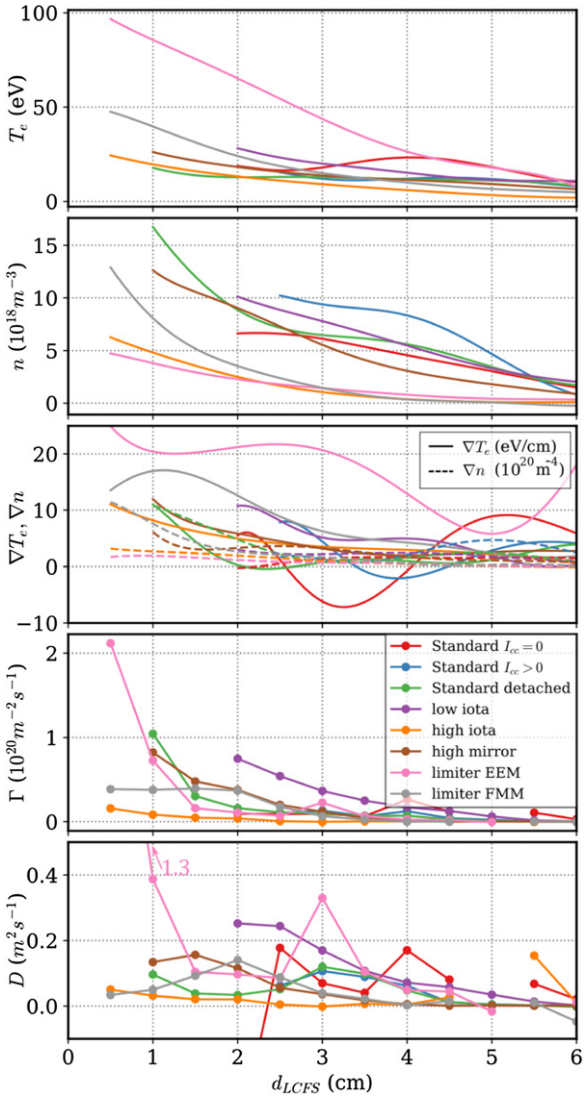

Figure 9. Radial profiles of anomalous diffusion coefficient D and relevant key plasma quantities along probe path for various magnetic configurations.

further analysis focuses on qualitative rather than quantitative differences.

Similar to the results in section 3, the standard configuration results appear to behave differently from the other configurations. While all other experiments show a monotonic increase of T_e, n towards the LCFS, the red (and to a smaller degree the blue) curve feature a distinct local peak/profile flattening close to the transition between long and short connection length region (see figure 1) at $d_{LCFS} = 4$ cm, which is not affecting the transport levels. In general, diffusion coefficients obtained via $D = \Gamma_r/\nabla n$ with Γ_r due to turbulent transport are not larger than a few 0.1 m^2 s^{-1}.

5. Summary and conclusion

Reciprocating probe measurements in the SOL of W7-X have been performed such that both the stationary T_e, n profiles as well as an estimate for the turbulent radial particle flux Γ_r were obtained. The underlying density and potential fluctuations follow approximately a normal distribution, while the

cross phase between n and v_r is ≈ 0, maximizing Γ_r and implying an interchange-type character of fluctuations. However, in some situations the magnitude of v_r becomes small compared to individual potential fluctuations as multiple potential measurements can show highly coherent, in-phase fluctuations, which are not consistent with interchange-type turbulence.

Still, over a wide range of magnetic configurations and plasma conditions, a roughly linear relation of $\Gamma_r \sim \nabla p$ was found, agreeing with the hypothesis that the turbulent transport in the W7-X SOL originates locally due to the SOL gradients. In detail, systematic quantitative differences regarding the strength of the $\Gamma_r \sim \nabla p$ scaling are observed between different magnetic configurations, which we associate to the different v_r levels following the relation of fluctuations in different potential pins. A prominent exception from the $\Gamma_r \sim \nabla p$ relation occurs in the main island SOL in the standard configuration, where even for very flat local gradients a significant turbulent particle transport is seen. While different potential explanations for this behaviour are discussed, more solid insight will require additional experiments in the upcoming operation phase 2 of W7-X.

Finally, describing the SOL turbulent particle transport as a diffusive process, anomalous diffusion coefficients D of typically a few 0.1 $m^2\ s^{-1}$ have been determined. Even within uncertainties of up to 50% due to spectral filter choices and probe pin configurations, these values are smaller than typical tokamak experimental results or modelling assumptions [30, 32, 35, 37]. In EMC3-EIRENE modelling of W7-X, D is typically assumed between 0.5 $m^2\ s^{-1}$–1.5 $m^2\ s^{-1}$ to obtain plausible modelling results [36, 38, 39]. Therefore, the level of turbulent transport observed here advocates to use 0.5 $m^2\ s^{-1}$ or less in EMC3-EIRENE simulations.

Acknowledgments

This work has been carried out within the framework of the EUROfusion Consortium and has received funding from the Euratom research and training programme 2014–2018 and 2019–2020 under Grant Agreement No. 633053. The views and opinions expressed herein do not necessarily reflect those of the European Commission.

ORCID iDs

Carsten Killer https://orcid.org/0000-0001-7747-3066
Yann Narbutt https://orcid.org/0000-0002-6279-3670

References

[1] Eich T. *et al* (ASDEX Upgrade Team and JET EFDA Contributors) 2013 *Nucl. Fusion* **53** 093031
[2] Sun H.J., Wolfrum E., Eich T., Kurzan B., Potzel S. and Stroth U. 2015 *Plasma Phys. Control. Fusion* **57** 125011
[3] Moyer R.A., Cuthbertson J.W., Evans T.E., Porter G.D. and Watkins J.G. 1997 *J. Nucl. Mater.* **241–243** 633
[4] Carralero D. *et al* 2017 *Nucl. Fusion* **57** 056044
[5] Eich T., Manz P., Goldston R.J., Hennequin P., David P., Faitsch M., Kurzan B., Sieglin B. and Wolfrum E. 2020 *Nucl. Fusion* **60** 056016
[6] LaBombard B., Boivin R.L., Greenwald M., Hughes J., Lipschultz B., Mossessian D., Pitcher C.S., Terry J.L. and Zweben S.J. 2001 *Phys. Plasmas* **8** 2107
[7] Boedo J.A. *et al* 2001 *Phys. Plasmas* **8** 4826
[8] D'Ippolito D.A., Myra J.R. and Zweben S.J. 2011 *Phys. Plasmas* **18** 060501
[9] Manz P. *et al* 2015 *Phys. Plasmas* **22** 022308
[10] Fuchert G., Birkenmeier G., Ramisch M. and Stroth U. 2016 *Plasma Phys. Control. Fusion* **58** 054005
[11] Grenfell G., van Milligen B.P., Losada U., Ting W., Liu B., Silva C., Spolaore M. and Hidalgo C. 2018 *Nucl. Fusion* **59** 016018
[12] Ida K. *et al* 2015 *Nucl. Fusion* **55** 013022
[13] Zoletnik S. *et al* (W7-X Team) 2019 *Plasma Phys. Control. Fusion* **62** 014017
[14] Killer C., Shanahan B., Grulke O., Endler M., Hammond K. and Rudischhauser L. (W7-X Team) 2020 *Plasma Phys. Control. Fusion* **62** 085003
[15] Barbui T. *et al* (W7-X Team) 2020 *Nucl. Fusion* **60** 106014
[16] Nold B., Conway G.D., Happel T., Müller H.W., Ramisch M., Rohde V. and Stroth U. (the ASDEX Upgrade Team) 2010 *Plasma Phys. Control. Fusion* **52** 065005
[17] Zweben S.J., Boedo J.A., Grulke O., Hidalgo C., LaBombard B., Maqueda R.J., Scarin P. and Terry J.L. 2007 *Plasma Phys. Control. Fusion* **49** S1
[18] Ricci P. and Rogers B.N. 2009 *Phys. Plasmas* **16** 062303
[19] Nicolai D. *et al* 2017 *Fusion Eng. Des.* **123** 960 Proc. 29th Symp. on Fusion Technology (SOFT-29) (Prague, Czech Republic, 5–9 September 2016)
[20] Killer C. *et al* (W7-X Team) 2019 *Nucl. Fusion* **59** 086013
[21] König R. *et al* 2002 *Plasma Phys. Control. Fusion* **44** 2365
[22] Geiger J. *et al* (the W7-X Team) 2021 Confinement and equilibrium with internal islands in a configuration scan with respect to iota in W7-X *2020 IAEA Fusion Energy Conf.* (10-15 May 2021 Nice, France) (https://conferences.iaea.org/event/214/contributions/17520/)
[23] Stangeby P.C. 2000 *The Plasma Boundary of Magnetic Fusion Devices* (Boca Raton, FL: CRC Press)
[24] Hutchinson I.H. 2002 *Principles of Plasma Diagnostics* (Cambridge: Cambridge University Press)
[25] Killer C. *et al* (W7-X Team) 2019 *Plasma Phys. Control. Fusion* **61** 125014
[26] Drews P. *et al* 2019 *Nucl. Mater. Energy* **19** 179
[27] Kraemer-Flecken A. *et al* 2019 *Plasma Phys. Control. Fusion* **61** 054003
[28] Rafiq T., Kleiber R., Nadeem M. and Persson M. 2002 *Phys. Plasmas* **9** 4929
[29] Shanahan B., Dudson B. and Hill P. 2018 *J. Phys.: Conf. Ser.* **1125** 012018
[30] Garcia O.E., Pitts R.A., Horacek J., Nielsen A.H., Fundamenski W., Graves J.P., Naulin V. and Rasmussen J.J. 2007 *J. Nucl. Mater.* **363–365** 575
[31] Naulin V. 2007 *J. Nucl. Mater.* **363–365** 24
[32] Manz P. *et al* 2020 *Phys. Plasmas* **27** 022506
[33] Feng Y., Sardei F. and Kisslinger J. 1999 *J. Nucl. Mater.* **266–269** 812
[34] Feng Y. *et al* 2014 *Contrib. Plasma Phys.* **54** 426
[35] Lunt T., Carralero D., Feng Y., Birkenmeier G., Müller H.W., Müller S. and Wischmeier M. 2015 *J. Nucl. Mater.* **463** 744
[36] Effenberg F. *et al* (W7-X Team) 2017 *Nucl. Fusion* **57** 036021
[37] Rozhansky V., Kaveeva E., Molchanov P., Veselova I., Voskoboynikov S., Coster D., Counsell G., Kirk A. and Lisgo S. 2009 *Nucl. Fusion* **49** 025007
[38] Winters V.R. *et al* 2021 *Plasma Phys. Control. Fusion* **63** 045016
[39] Feng Y. *et al* (W7-X Team) 2021 *Nucl. Fusion* **61** 086012